Renewable Energy 206 (2023) 1–12

Contents lists available at ScienceDirect

Renewable Energy

journal homepage: www.elsevier.com/locate/renene

Flow and heat transfer analysis of a gas–particle fluidized dense suspension in a tube for CSP applications

J.I. Córcoles [a,b], M. Díaz-Heras [a,b], M. Fernández-Torrijos [c], J.A. Almendros-Ibáñez [a,b,*]

[a] Universidad de Castilla-La Mancha, E.T.S. de Ingenieros Industriales, Dpto. de Mecánica Aplicada e Ingeniería de Proyectos, Campus universitario s/n, 02071, Albacete, Spain

[b] Universidad de Castilla-La Mancha, Renewable Energy Research Institute, Section of Solar and Energy Efficiency, C/ de la Investigación s/n, 02071, Albacete, Spain

[c] Universidad Carlos III de Madrid, ISE Research Group, Thermal and Fluid Engineering Department, Avda. de la Universidad 30, 28911 Leganés, Madrid, Spain

ARTICLE INFO

Keywords:
Concentrating solar power
Fluidized bed
Numerical simulation

ABSTRACT

This work presents a numerical study of the flow of particles in a gas–particle fluidized dense suspension for CSP applications using the Multi-Phase Particle in Cell (MP-PIC) method, implemented in CPFD-Barracuda software. The study covers two different numerical simulations. The first is a cold and isothermal model in which the fluctuations and control of the mass flow of particles ascending along the vertical tube was studied. In the second, a high-temperature boundary condition was imposed on the external surface of the tube and the energy equation was solved. In this second case, the heat transfer coefficient between the inner surface of the tube and the particles was numerically computed.

The numerical results in the cold model are highly consistent with experimental data available in the literature (with values up to 150 kg/h and differences of approximately ±10 kg/h) and underline the significant impact of the pressure at the bottom of the bed and of the aeration flow rate on the mass flow of particles. The results of the non-isothermal case present heat transfer coefficients in the range of 300–400 $W/(m^2 K)$ with transient fluctuations during the fluidization process. These fluctuations may be an influence on the mechanical damage of the tube, which is exposed to high levels of concentrated irradiation.

1. Introduction

In the worldwide energy context, the use of renewable energies is becoming a key factor in tackling the climate crisis caused by the greenhouse effect on the planet. According to the data published by the International Energy Agency (IEA) [1], for the period 2021–2026, an average annual addition of renewable installed capacity for electricity production of 304.8 GW is expected, although 548.0 GW will be needed for a net zero emissions scenario. These data result in an accumulated installed capacity of 6206.3 GW in the net zero scenario. These data involve an acceleration in the renewable energy penetration of almost 60% compared with the data of the five previous years. Worldwide installed capacity of one particular source, Concentrating Solar Power (CSP), will grow 100%, increasing from 6.4 GW installed in 2021 up to 13.1 GW, reaching the net zero emissions objective.

One of the main limitations of current commercial CSP plants installed all around the world is the limitation in the maximum operating temperature, which cannot exceed 565 °C when using molten salts as the Heat Transfer Fluid (HTF) in a solar central receiver [2]. This drastically limits the maximum efficiency of the thermodynamic cycle and reduces the competitiveness of the plant compared with other technologies. For 2025, different sources have established a maximum temperature objective of 900 °C [3] in CSP plants with a central tower and of above 700 °C [2] in third-generation CSP plants. To reach this objective, it is necessary to change the HTF, with one of the widely studied alternatives in recent years being the use of solid particles, such as sand or SiC, as the HTF and energy storage media [4,5]. Although it seems clear that the use of solid particles may overcome the drawback of the temperature limitation in CSP plants, there is no agreement on the fluid–particle technology employed as a solar receiver and storage, as there are a variety of proposed technologies, which can be classified into two main groups: direct and indirect systems. In the former, the solar irradiation is directly concentrated on the particles, whereas, in the latter, the particles are heated up by the heat transferred from a surface that is externally irradiated.

Among direct systems, we can distinguish between: (1) Free Falling Particles (FFP), in which a particle curtain is gravity falling in the rear

* Corresponding author at: Universidad de Castilla-La Mancha, E.T.S. de Ingenieros Industriales, Dpto. de Mecánica Aplicada e Ingeniería de Proyectos, Campus universitario s/n, 02071, Albacete, Spain.

E-mail address: jose.almendros@uclm.es (J.A. Almendros-Ibáñez).

https://doi.org/10.1016/j.renene.2023.02.004
Received 19 October 2022; Received in revised form 25 January 2023; Accepted 3 February 2023
Available online 6 February 2023

wall of a directly irradiated cavity [6], (2) Centrifugal Particle Receiver (CPR), where a film of particles is moving downward in the internal wall of a rotating cylinder that is directly irradiated through one aperture [7] and (3) Fluidized bed + Beam Down reflector (FB+BD), where a bubbling fluidized bed of particles is directly concentrated by a secondary beam-down reflector [8,9]. In general, direct systems have the advantage of increasing their efficiency as they avoid the use of intermediate surfaces. In contrast, the control of these systems is more complicated, as they are typically exposed to atmospheric conditions and the wind notably influences the flow control of the system [10]. The use of a fluidized bed enables us to operate with different materials with a wider particle size distribution compared with the other direct systems. In indirect systems, a dense suspension of particles is fluidized and moved up through the interior of a tube that is externally irradiated, and the heat is transferred to the particles through the tube thickness.

This research line includes a number of different experimental works. Boissiere et al. [11], in a cold experimental facility, studied the flow of SiC particles through two vertical tubes of 2.16 m length and 34 mm i.d. The bottom of both tubes were immersed in a pressurized bottom bubbling fluidized bed. They observed an even flow distribution between both tubes of approximately 52 kg/h with an overpressure at the bed bottom of 248 mbar. The authors concluded it was necessary to include an aeration flow rate in vertical tubes to maintain a stable particle flow rate. Subsequently, Benoit et al. [12] experimentally tested a similar facility under solar irradiation conditions, reaching maximum temperatures of up to 723 °C in the particles, with solar flux densities up to 393 kW/m^2 in a sun oven of 10 kW_{th}. Benoit et al. [12] measured the heat transfer coefficient and observed a clear linear relationship between the heat transfer coefficient and the solid mass flux of particles ascending in the tube, rising approximately from 600 to 1200 $W/(m^2\,K)$ when the flux of particles increases from 20 to 50 $kg/(m^2\,s)$. The authors proposed the following relationship:

$$h_w = 16.56\,\frac{m^2\,s}{kg}\,\frac{\dot{m}_{p,f}}{A_t} + 325.6\,\frac{kg}{m^2\,s} \tag{1}$$

where $\dot{m}_{p,f}$ is the mass flow rate of particles ascending in the tube and A_t the cross sectional area of the tube. The correlation is valid in the range of $9.5\,kg/(m^2\,s) \le \dot{m}_{p,f}/A_t \le 45.1\,kg/(m^2\,s)$ for a tube with an internal diameter of $d = 34$ mm. Note that Eq. (1) should be carefully applied to experimental conditions other than those proposed by Benoit et al. [12]. In another work, Jiang et al. [13] observed similar values for the heat transfer coefficient in countercurrent fluidized bed configuration (the particles moving down within an i.d. 40 mm vertical tube) with quartz sands Geldart B particles for the same range of mass-flux of particles.

One of the main problems in indirect systems is the proper control of the up-flow rate of particles in the tube and the appearance of bubbles and slugs along the tube length. To achieve a high heat transfer rate from the wall to the particles, it is necessary to ensure a continuous and stable contact between the solid particles and the internal wall of the tube. In this sense, previous works [11,12] used Geldart A particles (SiC particles with a mean particle size of 64 mm) combined with low air flow rates to obtain small bubbles and avoid bubble coalescence during the fluidization process, as occurs with larger Geldart B particles [14]. Additionally, in a recent study, Deng et al. [15] proposed the use of Bubble Rupture Promoters (BRP) to mitigate the appearance of slugs in large tubes with a small diameter. The authors observed that the appearance of slugs limited the heat transfer coefficient to below $200\,W/(m^2\,K)$, while the use of BRP maintained the coefficient at over $600\,W/(m^2\,K)$.

There are few numerical studies on gas–particle dense suspension in a tube. Benoit et al. [16] numerically studied a dense particle suspension in a tube using a two-fluid model (implemented in the NEPTUNE-CFD software). They imposed a heat transfer coefficient as boundary condition, obtained from the experimental results of the same authors [12], although the outlet particle temperature was underestimated. In this way, they increased the heat transfer coefficient to match the experimentally measured outlet particle temperature. They also analysed the time-average-cross-sectional profiles of air velocity and particle fraction and observed, in the region of the heated particles, a great impact of the temperature on these profiles. As the temperature increased, the particle volume fraction was reduced and the recirculation was more intense. Deng et al. [15], with the same NEPTUNE software, numerically studied the influence of BRP on the flow of particles. They studied an isothermal model (a tube of 5 m length) and observed that BRP promotes a more uniform solid fraction along the tube. More recently, Jiang et al. [17] used the MP-PIC approach to numerically study the flow of particles in a countercurrent fluidized bed of quartz sand particles with a mean particle size of $d_p = 198.3$ mm. They studied the solid holdup distribution, axial particle velocity and bubble size, velocity and distribution, concluding that the numerical simulations permits aspects of the flow that are not possible to measure in an experimental facility to be viewed in detail. Additionally, the MP-PIC approach properly predicted the performance of the bed.

The aim of the present work is to present a detailed numerical analysis of the flow and heat transfer of a dense suspension of externally heated fluidized particles. In particular, the main aspects studied in this work are: (1) the variation of the mass flow of particles with boundary conditions, and (2) the fluctuation of the heat transfer coefficient from the wall due to the non-homogeneous flow of particles in the system. To perform the study, the Multi-Phase Particle in Cell (MP-PIC) method, implemented in the CPFD-Barracuda software, was used [18,19]. The experimental conditions of [11,12] were reproduced and the impact of the grid size and time step on the results was also analysed.

2. Governing equations and model description

This section briefly describes the governing equations used in the MP-PIC method. These have been documented in the literature [20], and the reader is referred to previous works of the authors [18,19] and references therein for a detailed description of the equations discussed.

In the absence of interphase mass transfer, the continuity (2) and momentum equations (3) are given by [21,22]:

$$\frac{\partial\left(\theta_f\,\rho_f\right)}{\partial t} + \nabla\cdot\left(\theta_f\,\rho_f\,\vec{u}_f\right) = 0 \tag{2}$$

where θ_f is the fluid volume fraction, ρ_f is the fluid density, u_f is the gas velocity; and

$$\frac{\partial\left(\theta_f\,\rho_f\,\vec{u}_f\right)}{\partial t} + \nabla\cdot\left(\theta_f\,\rho_f\,\vec{u}_f\,\vec{u}_f\right) = -\nabla p - \vec{F} + \theta_f\,\rho_f\,\vec{g} + \nabla\cdot\left(\theta_f\,\tau_f\right) \tag{3}$$

where p is the fluid pressure, $\vec{F}$ is the momentum exchange rate per volume between gas and particles, g is the gravity acceleration, and τ_f is the fluid stress tensor.

The variable $\vec{F}$ is computed as follows (Eq. (4)):

$$\vec{F} = \iiint f\,\left\{V_p\,\rho_p\left[D_p\left(\vec{u}_f - \vec{u}_p\right) - \frac{1}{\rho_p}\nabla p\right] + \vec{u}_{\vec{p}}\,\frac{dm_p}{dt}\right\} dV_p\,d\rho_p\,d\vec{u}_p\,dT_p \tag{4}$$

where f is the particle probability distribution function, V_p is the particle volume, ρ_p is the particle density, D_p is the drag function, u_p is the particle velocity, m_p is the particle mass, and T_p is the particle temperature.

The air density is computed using the ideal gas equation of state:

$$p = \rho_f\,R_g\,T \tag{5}$$

where R_g is the gas constant and T the absolute temperature.

The parameters for Equations (4) and (5) are listed in Table 1.

Large eddy simulation (LES) turbulence was used as the turbulence model. In this model, the large eddies are calculated from the flow

Table 1
Parameters of momentum and fluid and solid phase energy equations.

Momentum equation
$\frac{\partial f}{\partial t} + \nabla \cdot (f\,\vec{u}_p) + \nabla \vec{u}_p \cdot \left(f\,\frac{d\vec{u}_p}{dt} \right) = 0$ [24,25]
$\frac{d\vec{u}_p}{dt} = D_p\,(\vec{u}_f - \vec{u}_p) - \frac{1}{\rho_p}\nabla p - \frac{1}{\theta_p \rho_p}\nabla \tau_p + \vec{g}$
$\tau_p = \frac{P_s\,\theta_p^{\beta}}{\max\left[(\theta_{cp} - \theta_p), \varepsilon\,(1-\theta_p)\right]}$
Fluid-phase energy equation
$\vec{q} = -k_f \nabla T_f$
$S_h = \int\int\int f \left\{ m_p \left[D_p(\vec{u_p} - \vec{u_f})^2 - Cp_p \frac{dT_p}{dt} \right] - \frac{dm_p}{dt}\left[h_{pe} + \frac{1}{2}(\vec{u_p} - \vec{u_f})^2 \right] \right\} dm_p\, d\vec{u_p}\, dT_p$
Solid-phase energy equation
$Cp_p \frac{dT_p}{dt} = \frac{1}{m_p}\left(\frac{k_f\,Nu_f}{d_p} A_p\,(T_f - T_p) + \dot{Q}_{\text{rad}} \right)$

Table 2
Parameters of Wen–Yu drag model.

Wen–Yu drag model	
$D_p = 0.75\,C_d\,\frac{\rho_f\,\lvert\vec{u_f} - \vec{u_p}\rvert}{\rho_p\,d_p}$	
$C_d = \begin{cases} \frac{24}{Re}\theta_f^{-2.65} & \text{for } Re < 0.5 \\ \frac{24}{Re}\left(1 + 0.15\,Re^{0.687}\right)\theta_f^{-2.65} & \text{for } Re \le 0.5 \le 1000 \\ 0.44\,\theta_f^{-2.65} & \text{for } Re > 1000 \end{cases}$	
$Re = \frac{\rho_f\,\lvert\vec{u_f} - \vec{u_p}\rvert\,d_p}{\mu_f}$	

equations and the subgrid turbulence is captured through a model. Barracuda uses the subgrid scale (SGS) model [23], which calculates an eddy viscosity based on the notion that the effect of the SGS Reynolds stress increases transport and dissipation.

The fluid-phase energy equation obtained from the fluid total energy equation [26,27] is defined by (6):

$$\frac{\partial}{\partial t}\left(\theta_f \rho_f h_{fe}\right) + \nabla \cdot \left(\theta_f \rho_f h_{fe} \vec{u}_{\vec{f}}\right) = \theta_f \left(\frac{\partial p}{\partial t} + \vec{u}_{\vec{f}} \cdot \nabla p \right) + \Phi - \nabla \cdot (\theta_f \vec{q}) + \dot{Q} + \dot{q}_D + S_h \tag{6}$$

where h_{fe} is the fluid enthalpy, Φ is the viscous dissipation (neglected due to absence of energy source or chemical reactions), $\vec{q}$ is the fluid heat flux, $\dot{Q}$ is an energy source per volume, $\dot{q}_D$ is the enthalpy diffusion term associated with chemical reactions, and S_h is the conservative energy exchange from the particle phase to the fluid phase.

The parameters for Eq. (6) and energy equation for the solid-phase are listed in Table 1.

2.1. Drag model

To compute the drag force exerted on the particle (F_p)(Eq. (7)), the following equation is used:

$$\vec{F}_p = m_p\,D_p\,\lvert\vec{u_f} - \vec{u_p}\rvert \tag{7}$$

In the present study, the Wen-Yu drag model [28] was used. Previous studies [20,29] concluded that the influence of the drag model on the behaviour of the bed with Geldart A particles (bubbles sizes and velocities, distribution of the particle volume fraction, etc.) is negligible, with the proper selection of the mesh size being much more significant. Table 2 summarizes the main equations and variables for this model.

2.2. Heat transfer coefficients

In CPFD-Barracuda software, to compute the local fluid-to-wall heat transfer coefficient (h_w)(Eq. (8)), it is divided into two components [30], namely, the heat transfer coefficient of the gas (h_f) (Eq. (10)) and the heat transfer coefficient of the particles (h_p) (Eq. (11)), weighted by a function of the particle volume fraction at the wall (f_p). In Barracuda [18], the wall transfers energy to the fluid phase, which can then transfer energy to the particles, such that the heat is transferred from the walls to the particles through the fluid phase.

$$h_w = h_f + f_p\,h_p \tag{8}$$

$$f_p = 1 - e^{-10\,(\theta_p/\theta_{cp})} \tag{9}$$

$$h_f = \left(c_0\,Re_L^{n1}\,Pr^{n2} + c_1\right)\frac{k_f}{L} + c_2 \tag{10}$$

$$h_p = \left(c_3\,Re_p^{n3}\right)\frac{k_f}{d_p} \tag{11}$$

where θ_p is the particle volume fraction, θ_{cp} is the particle volume fraction at close packing, L is the cell length, Pr is the Prandtl number, k_f is the fluid thermal conductivity, d_p is the particle diameter, and c_0, c_1, c_2, c_3, n_1, n_2 and n_3 are the input model parameters. In this work, c_0, c_1, c_2 and c_3 had a value of 0.46, 3.66, 0 W/(m^{2}K) and 0.525, respectively, while n_1, n_2 and n_3 presented a value of 0.5, 0.33 and 0.75, respectively. These coefficients are the default values proposed by the CPFD-Barracuda software [30–32].

The Reynolds numbers in Eqs. (10) and (11) are defined as follows:

$$Re_L = \frac{\rho_f\,u_f\,L}{\mu_f} \tag{12}$$

$$Re_p = \frac{\rho_f\,u_f\,d_p}{\mu_f} \tag{13}$$

where μ_f is the dynamic viscosity of the fluid and u_f is the local fluid velocity, directly computed from CPFD-Barracuda.

Heat transfer between the fluid phase and the particle phase is modelled by the fluid-to-particle heat transfer coefficient (h_{fp}), defined as follows:

$$h_{fp} = (c_4 Re^{n_4} Pr^{0.33} + c_5)\frac{k_f}{d_p} + c_6 \tag{14}$$

where c_4, c_5, c_6 and n_4 are input coefficients with the default values of 0.37, 0.1, 0 W/(m^{2}K) and 0.6, respectively, which properly fit the experimental data of Turton et al. [33]

2.3. Radiative heat transfer

The radiative heat transfer was computed according to the expression of the radiation exchange between two parallel partly reflecting surfaces [34]:

$$\dot{Q}_{\text{rad}} = \left(\pi\,d\,L_{\text{heat}}\right)\,F_{wp}\,\frac{\sigma\left(T_w^4 - \bar{T}_p^4\right)}{\frac{1}{\varepsilon_p} + \frac{1}{\varepsilon_w} - 1} \tag{15}$$

where L_{heat} is the length of the heated wall, T_w is the wall temperature (700 °C), $\bar{T}_p$ is the mass-weighted temperature of the particles and ε_w and ε_p are the wall and particle emissivity, respectively. F_{wp} is the view factor between the wall and the particles in the adjacent cells. $\dot{Q}_{\text{rad}}$ is added as a source term in the energy equation for the solid phase, as shown in Table 1.

3. Model setup

In the present study, two cases were analysed, a cold model and a hot model. The numerical domain of this work reproduces the experimental facility employed by Boissiere et al. [11] and Benoit et al. [12],

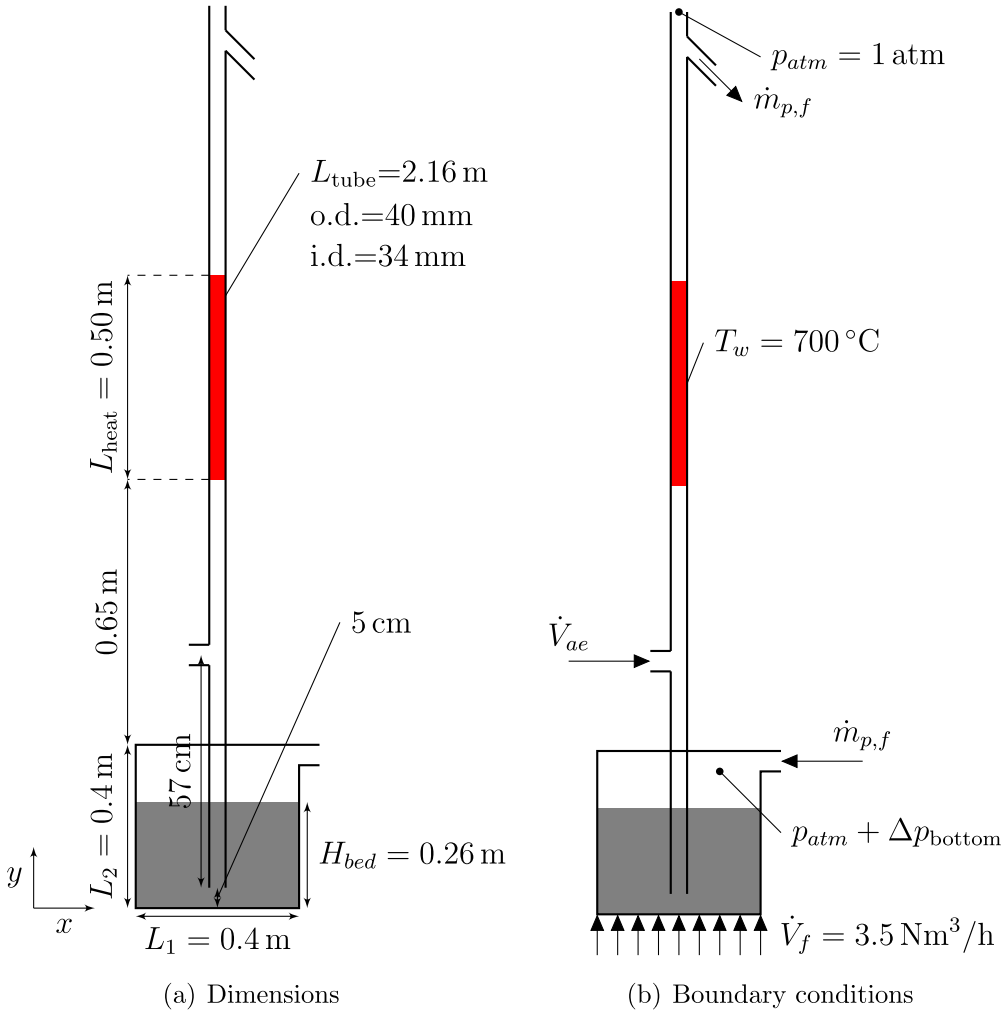

Fig. 1. Scheme of the experimental facility and conditions of Boissiere et al. [11]. The third bed dimension is L_3 = 0.2 m.

who experimentally studied the up-flow of particles under isothermal cold conditions and with high temperatures. The main dimensions and boundary conditions are shown in Fig. 1. This consists of a rectangular pressurized bubbling fluidized bed at the bottom, with a cross-sectional area of 0.2 m × 0.4 m, and a height of 0.4 m. The bed is filled with 30 kg of SiC particles with a Sauter diameter of d_{32} = 64 μm and a real density of 3220 kg/m^3. The initial particle volume fraction at close packing (θ_{cp}) and sphericity (Ψ_p) were 0.43 and 0.7, respectively. In the boundary conditions of this work, the mass flow rate of particles leaving the system from the top right outlet, $\dot{m}_{p,f}$, was imposed as the inlet boundary condition in the inlet of the bottom bed. The aeration flow rate ($\dot{V}_{ae}$) was varied between 0 and 150 NL/h and the overpressure at the bottom was varied in the range of 31.7 − 34.7 kPa. Boissiere et al. [11] used two similar tubes in parallel to corroborate the even distribution of the particles in both tubes. In the present study, only one tube was included to reduce the computational cost. The separation between the tube inlet and the bottom of the fluidized bed was 5 cm.

To analyse the influence of the time step and grid size, additional simulations were performed on the cold model. The initial and boundary conditions to perform the grid analysis were those of a case reproducing the experimental conditions of Boissiere et al. [11] as we now explain. Regarding the time step analysis, two time steps (10^{-3} s and 10^{-4} s) were studied. In both cases, three grid sizes were analysed (2.25×10^5, 4.50×10^5 and 9.00×10^5 real cells). In all the grids, uniform mesh (Fig. 2) was defined in all directions. Table 3 details information on the grids used.

Table 3
Cell and computational parameters for the cases studied.

Case	Time step [s]	$N_{\text{comput. parcels}}$	N_{cells}	$N_{\text{iterations}}$	Comput. time [s]
1	10^{-3}	8.49×10^5	2.25×10^5	3.05×10^5	8.87×10^4
2	10^{-3}	1.76×10^6	4.50×10^5	4.09×10^5	1.89×10^5
3	10^{-3}	3.33×10^6	9.00×10^5	3.97×10^5	2.27×10^5
4	10^{-4}	8.49×10^5	2.25×10^5	3.00×10^6	7.30×10^5
5	10^{-4}	1.76×10^6	4.50×10^5	3.00×10^6	8.77×10^5
6	10^{-4}	3.33×10^6	9.00×10^5	3.01×10^6	1.58×10^6

Regarding the cold model, compressible air enters at the bottom inlet to fluidize the bed, with an isothermal flow temperature of 300 K. The bottom bed was fluidized with an air flow rate of 3.5 Nm^3/h which corresponds to 1.2 times the minimum bubbling velocity (u_{mf}). The mass flow rate at the top outlet was equal to the mass flow rate at the bottom inlet. Inside the tube, there was an aeration air flow rate ($\dot{V}_{ae}$) of 150 NL/h at a height of 57 cm from the tube inlet. Different simulations were carried out, varying the overpressure at the bottom of the bed (Δp_{bottom}), ranging between 31.7 kPa and 34.7 kPa. The fluidized bed at the bottom was pressurized with a gauge pressure of the corresponding Δp_{bottom}. The pressure at the outlet of the tube was 1 atm. Moreover, to analyse the influence of the aeration flow rate, three additional cases were considered, modifying $\dot{V}_{ae}$ (0, 40 and 80 NL/h) at a Δp_{bottom} of 32.2 kPa. An adiabatic condition was defined for all walls. A non-slip condition was defined at the walls for the gas. A value of 0.85 was defined for both the normal to wall momentum retention and tangent

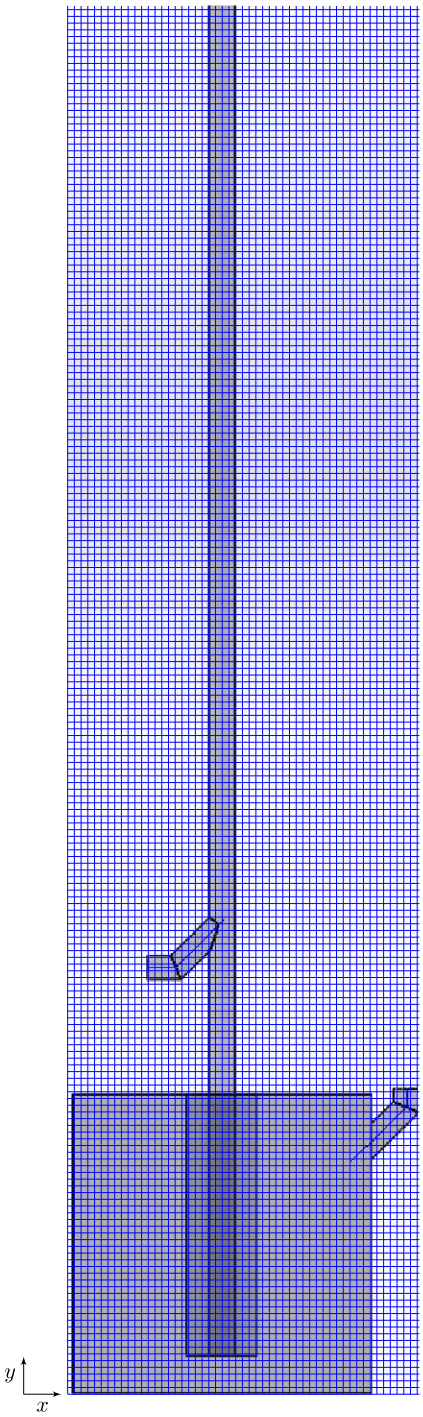

Fig. 2. Detail of the grids studied.

to wall momentum retention [35], as well as a diffuse bounce of 5 [36]. To compute particle to particle interaction, the values for the constants P_s (1), ϵ (10^{-8}) and β (3)(Table 1) were kept to the default [20,37]. For each case studied, the simulation time was 300 s. For the grid and time step sensitivity analysis, of the cases defined, the simulated one had an air flow rate of 3.5 Nm^3/h, $\dot{V}_{ae}$ of 150 NL/h and overpressure at the bottom of the bed Δp_{bottom} of 32.2 kPa.

For the hot model, the parameters defined were similar to those described for the cold model. A numerical simulation was performed, considering Δp_{bottom} of 32.2 kPa and an aeration flow rate of 150 NL/h. The previous cold model was slightly modified to also solve the energy equations. In this case, we reproduced the experimental conditions with solar irradiation on the external surface of the tube proposed by Benoit et al. [12], who used a solar furnace of 1 MW. They performed several experiments, where a tube was irradiated along 0.5 m in height, achieving heat fluxes onto the surface of the tube of between 213 and 393 kW/m^2. Benoit et al. [12] reported wall temperatures of around 700 °C on the external surface of the tube, with maximum variations of 150 °C around the tube, measuring the maximum temperatures on the side of the tube directly exposed to the solar irradiation. In CPFD-Barracuda, it is not possible to impose a heat flux boundary condition on the surface of the tube to simulate the solar irradiation on the heated height of 0.5 m. Instead, a constant temperature of 700 °C was fixed as the boundary condition on the tube surface (highlighted in red in Fig. 1), and the initial temperature of the particles at the bed bottom was set to 500 °C, following the experimental conditions of Benoit et al. [12], who used electrical resistances to preheat these particles to the desired temperature.

Tables 4 and 5 show the main parameters for the numerical simulation.

4. Grid and time step analysis

To check the sensibility of the numerical model with the time step and with the mesh size, six different cases were studied, with two different time steps ($\Delta t = 10^{-3}$ s and 10^{-4} s) and three different numbers of cells ($N_{\text{cells}} = 2.25 - 4.50 - 9.00 \times 10^5$). Table 3 summarizes the number of numerical iterations and the computational cost for each case. It can clearly be seen that the computational time notably increases for the smallest time step ($\Delta t = 10^{-4}$ s), being approximately one order of magnitude higher than the equivalent case for $\Delta t = 10^{-3}$ s. A criterion to choose the correct combination of time step and cell size to ensure the accuracy of the numerical model, without increasing the computational time, is the CFL (Courant–Friedrichs–Lewy) factor. This parameter is defined as follows:

$$CFL = \frac{\Delta t\, u}{\Delta x} \tag{16}$$

and a value of $0.8 \leq CFL \leq 1.5$ is recommended to maintain a compromise between stability, accuracy, and speed of calculation [18,19]. Fig. 3 shows the CFL factor during 1 s of numerical simulation for the six cases studied. It can clearly be observed that the three cases with the smallest time step ($\Delta t = 10^{-4}$ s) present a very low value for the CFL factor, being below or around 0.2, which indicates a high computational cost with no increase in accuracy. The cases with $\Delta t = 10^{-3}$ s and $4.50 - 9.00 \times 10^5$ cells show values in the recommended range. In these cases, the software automatically reduces the time step when $CFL > 1.5$ to maintain its value in the recommended range, as seen in Fig. 3.

For additional comparison, Fig. 4 shows the absolute pressure measured at two different heights in the centre of the tube: $y = 0.94$ m and $y = 1.94$ m during 1 s of numerical simulation. There are no notable differences between the different cases and the global behaviour of the bed is similar, regarding both time step and cell size.

Given the results obtained in the grid and time step analysis, the results presented in the following section were obtained with $\Delta t = 10^{-3}$ s and $N_{\text{cells}} = 4.50 \times 10^5$ (Case 2) to ensure a reasonable computational cost and accuracy in the results. In the non-isothermal case, the time step was reduced to $\Delta t = 2 \times 10^{-4}$ s, with the same number of cells, because the high thermal gradients did not allow a CFL factor to be maintained below the maximum recommended value of 1.5.

5. Numerical results of the isothermal case (cold model)

One of the key aspects of the proposed system is the proper control of the flow of particles in the tube. Boissiere et al. [11] and Benoit et al. [12] proposed the use of small SiC Geldart A particles (with a mean Sauter diameter of $d_{32} = 64\,\mu$m). The fluidization of this type

Table 4
Initial conditions for the numerical simulations. In the particle specific heat expression, the temperature should be included in Kelvin and $a = -512.5$, $b = 6.36$, $c = -0.010$, $d = 8.01 \times 10^{-6}$ and $e = -2.4 \times 10^{-9}$.

	Cold model	Hot model
Particle type	SiC	SiC
Particle diameter (d_p, μm)	64	64
Particle density (ρ_p, kg m^{-3})	3220	3220
Particle specific heat (Cp_p, J kg^{-1} K^{-1}) [38]	–	$a + bT + cT^2 + dT^3 + eT^4$
Particle thermal conductivity (k_p, W m^{-1} K^{-1})	–	65
Initial particle volume fraction at close packing (θ_{cp})	0.43	0.43
Particle sphericity (Ψ_p)	0.7	0.7

Table 5
Boundary conditions for the numerical simulations.

		Cold model	Hot model
Inlet	Gas velocity (u_f, Nm^3/h)	3.5	3.5
	Fluid temperature (T_f, K)	298.15	298.15
	Particle temperature (T_p, K)	298.15	773.15
Bottom of the bed	Over pressure (Δp_{bottom}, kPa)	31.7, 31.8, 31.9, 32.2, 32.7, 33.7, 34.7	32.2
Outlet	Pressure outlet (P_{out}, Pa)	101,325	101,325
Aeration	Flow rate ($\dot{V}_{ae}$, NL/h)	0, 40, 80, 150	150
Walls	Wall bed temperature (T_{wb}, K)	Adiabatic	Adiabatic
	Tube surface constant temperature (T_s, ° C)	298.15	700
	Gas	Non-slip	Non-slip
	Particle to wall interaction:		
	Normal-to-wall retention coefficient	0.85	0.85
	Tangent-to-wall retention coefficient	0.85	0.85
	Diffuse bounce	5	5

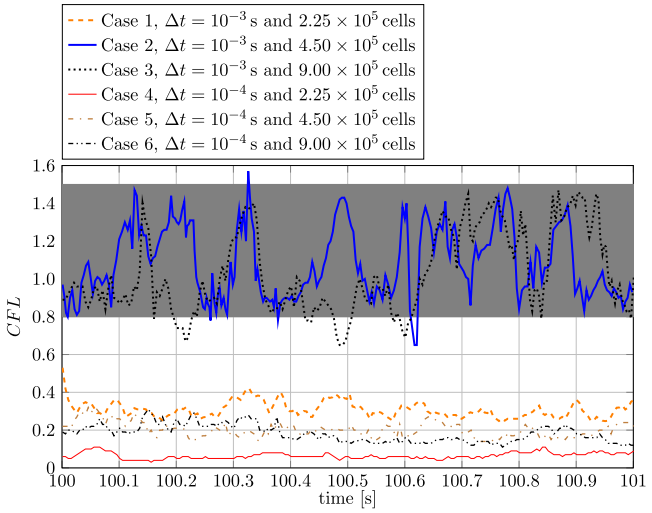

Fig. 3. Evolution of CFL factor for the six cases studied. Grey indicates the recommended range.

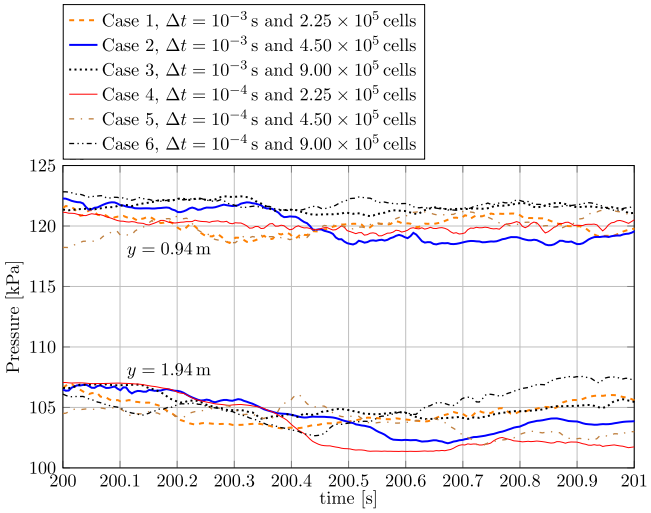

Fig. 4. Evolution of the absolute pressure at the different axial positions in the center of the tube for the six cases studied.

of particle is smooth with small bubbles that do not coalesce, which allows for a more homogeneous particle flow along the vertical tube. In addition, the possibility of slugs appearing is reduced, compared with other particle types, such as Geldart B particles. Nevertheless, no flow of a dense suspension of fluidized particles is continuous and homogeneous in nature, as is the case of a liquid flow. For a certain types of particles, the flow should be controlled by two external parameters: the pressure in the bottom bed and the aeration flow in the tube.

5.1. Influence of the bottom pressure

As a general view of the hydrodynamic process, Fig. 5 shows the particle volume fraction (θ_p) in the entire domain. It can be seen that most of the vertical tube is filled with close packing groups of particles (in red, with $\theta_p \sim 0.5$) although there are also some regions of low particle concentration. Fig. 5 shows that a low voidage region is formed during the first 0.5 s in the region close and over the entrance of the aeration flow. Thes low voidage regions, or slugs, ascend along the tube over the following 0.5 s. Additionally, close to the exit of the particles, voidage is reduced. The location of the aeration flow at the bottom left-hand side of the geometry and the exit of the particles at the top right-hand part of the tube seems to encourage small regions of low particle concentration (bubbles) appearing along the vertical tube on the left-hand side of the computational domain. The righ-hand side is always filled with particles at close packing.

Fig. 6 shows the numerical results obtained for the same experimental conditions as those used by Boissiere et al. [11]. This figure shows the evolution of the mass of particles collected at the outlet of the tube

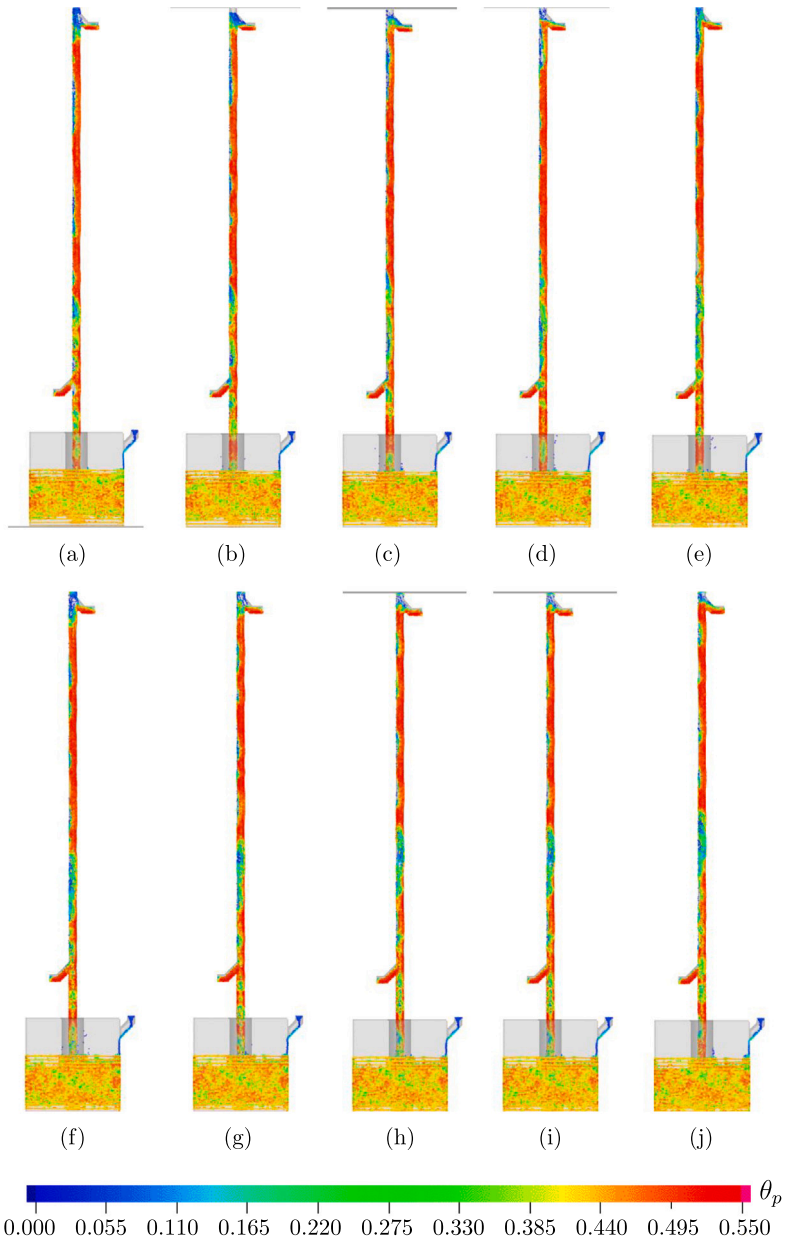

Fig. 5. Snapshots of particle volume fraction, θ_p between $t = 100.1$ and $t = 101.0$ s with $\Delta t = 0.1$ s between figures for $\Delta p_{\text{bottom}} = 32.2$ kPa.

over 5 min of numerical simulation. It was numerically computed as follows:

$$m_p = \int_0^t \int \dot{m}_{p,f} \, \mathrm{d}A_t \, \mathrm{d}t \tag{17}$$

It can clearly be seen that there is a threshold value of the overpressure at the bottom that establishes a continuous flow. For overpressures below 31.8 kPa, after a transient initial period, the mass of particles remains approximately constant, which indicates that there is no flow of particles. For higher values of Δp_{bottom}, after around the first 10 s, the mass of particles increases approximately linearly in time. The higher the overpressure, the higher is the slope of the line.

Fig. 7 shows the up-flow of particles, $\dot{m}_{p,f}$, which was computed as the slope of a minimum square fitting of the results presented in Fig. 6, discarding the first 10 s in each case due to the initial transient period. The same figure presents the experimental data reported by Boissiere et al. [11]. The first clear discrepancy is the difference in the value of the overpressure in the bottom bed, Δp_{bottom}, which is approximately 5 kPa higher in the numerical results of this work. These differences could be attributed to the differences in the real experimental facility and the numerical geometry. The numerical simulation of this work does not include the complete experimental facility. Specifically, the hopper and the recirculation system for the particles are not included, which may affect the pressure variations in the tube. Nevertheless, the relative difference is below 20% and the values of $\dot{m}_{p,f}$ are very similar in both cases. The numerical results in the present work indicate that the up-flow of particles increases slowly for higher overpressure values, although these values were not reached by Boissiere et al. [11]. There are two different regions in Fig. 7. In the first region, the up-flow of particles increases with the overpressure at the bottom with a rate of approximately 25 (kg/h)/kPa in both experimental and numerical data. This first region is very narrow and covers a range of approximately 0.5 kPa over the minimum pressure to move the particles along the tube. In the second region, the numerical data show that $\dot{m}_{p,f}$ increases linearly with the overpressure at a lower rate of approximately 0.5 (kg/h)/kPa.

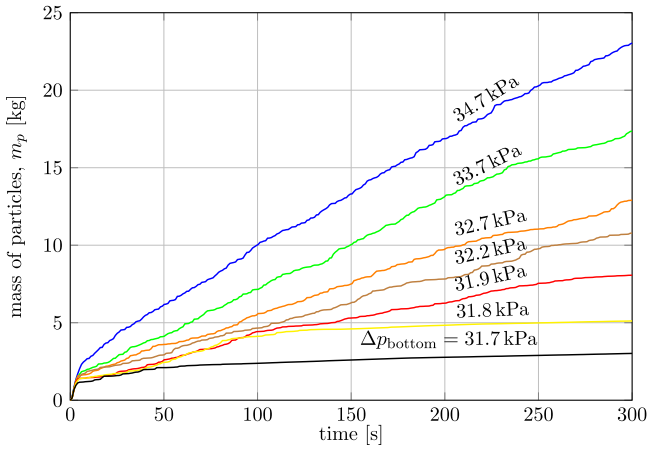

Fig. 6. Total mass of particles at the exit of the tube for different overpressures in the bottom bed.

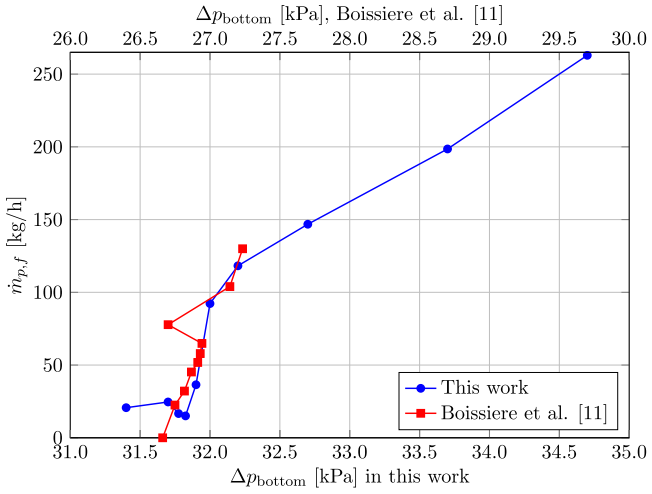

Fig. 7. Up-flow of particles at the exit of the vertical tube as a function of the bottom overpressure.

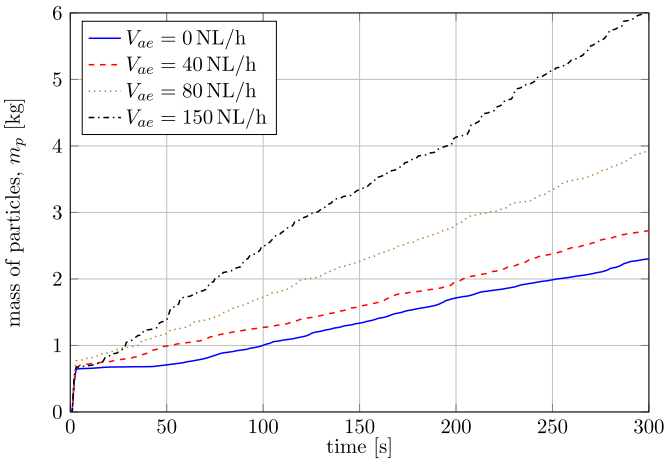

(a) Total mass of particles

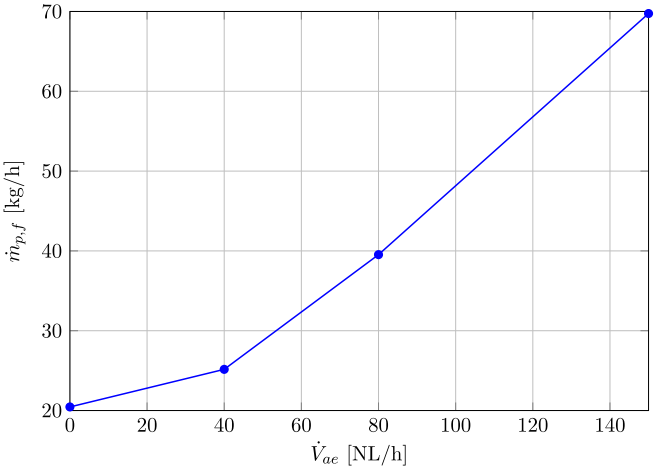

(b) Up-flow of particles

Fig. 8. Total mass of particles (a) and up-flow of particles (b) at the exit of the tube for different aeration flow rates and $\Delta p_{\text{bottom}} = 32.2$ kPa.

5.2. Influence of the aeration flow rate

Fig. 8 shows the influence of the aeration flow rate on the total mass of particles transported in the tube, for the case with an overpressure at the bottom of $\Delta p_{\text{bottom}} = 32.2$ kPa. Fig. 8(a) shows the total mass of particles at the exit of the bed, which was computed according to Eq. (17), for different values of the aeration flow rate ($\dot{V}_{ae}$), while Fig. 8(b) shows the up-flow of particles $\dot{m}_{p,f}$ vs $\dot{V}_{ae}$. It can be clearly observed that the mass of particles vertically transported through the tube increases with the aeration flow rate in the tube. Boissiere et al. [11] observed fluctuations in the up-flow of particles, related to fluctuations in the pressure at the bottom of the bed when the aeration flow rate is low. They then established a value of $V_{ae} = 150$ NL/h to obtain a stable and steady $\dot{m}_{p,f}$. This effect cannot be observed in the numerical simulations because the Δp_{bottom} is fixed as a boundary condition in the problem. If this overpressure is maintained constant, the up-flow of particles clearly increases.

6. Numerical results of the non-isothermal case (hot model)

In the non-isothermal case, the energy equations for gas and particles were solved. In this case, the experimental temperatures in Benoit et al. [12] were reproduced; the particles were preheated up to 500 °C and the wall temperature was fixed to 700 °C. For the results presented in the present work, the case with $\Delta p_{\text{bottom}} = 32.2$ kPa was selected and an aeration flow rate of 150 NL/min. Fig. 9 shows a general overview of the particle motion and temperature along the heated section, with the length of the tube being between 1.05 and 1.55 m, as indicated in Fig. 1. Figs. 9(a)–(j) show the particle volume fraction θ_p, which varies along the tube height. Different regions of low particle concentration are observed and the motion is vigorous. The regions of the tube with low particle concentration may locally reduce the heat transfer coefficient between the internal wall and the solid particles, although the particle velocity is high and the period of time that the wall is not in contact with particles in motion seems to be very short. Figs. 9(k)–(t) show the particle temperature. The particles are heated as they ascend along the vertical tube, with more particles at high temperature being observed, around 800 K, at the end of the heated section.

Fig. 10 shows the increase in the particle temperature between the inlet (at $x = 1.05$ m) and the outlet (at $x = 1.55$ m) of the heated length of the tube over 250 s of numerical simulation. In this case, the initial condition for the particles was a temperature of $T = 500$ °C, while all the system was considered adiabatic, except for the surface of the tube between $x = 1.05$ m and $x = 1.55$ m. In the heated length of the tube a constant temperature of 700 °C was imposed. The results indicate high frequency oscillation in both temperatures, which is related to the intermittent nature of a group of fluidized particles ascending in a vertical tube. The temperature at $x = 1.05$ m

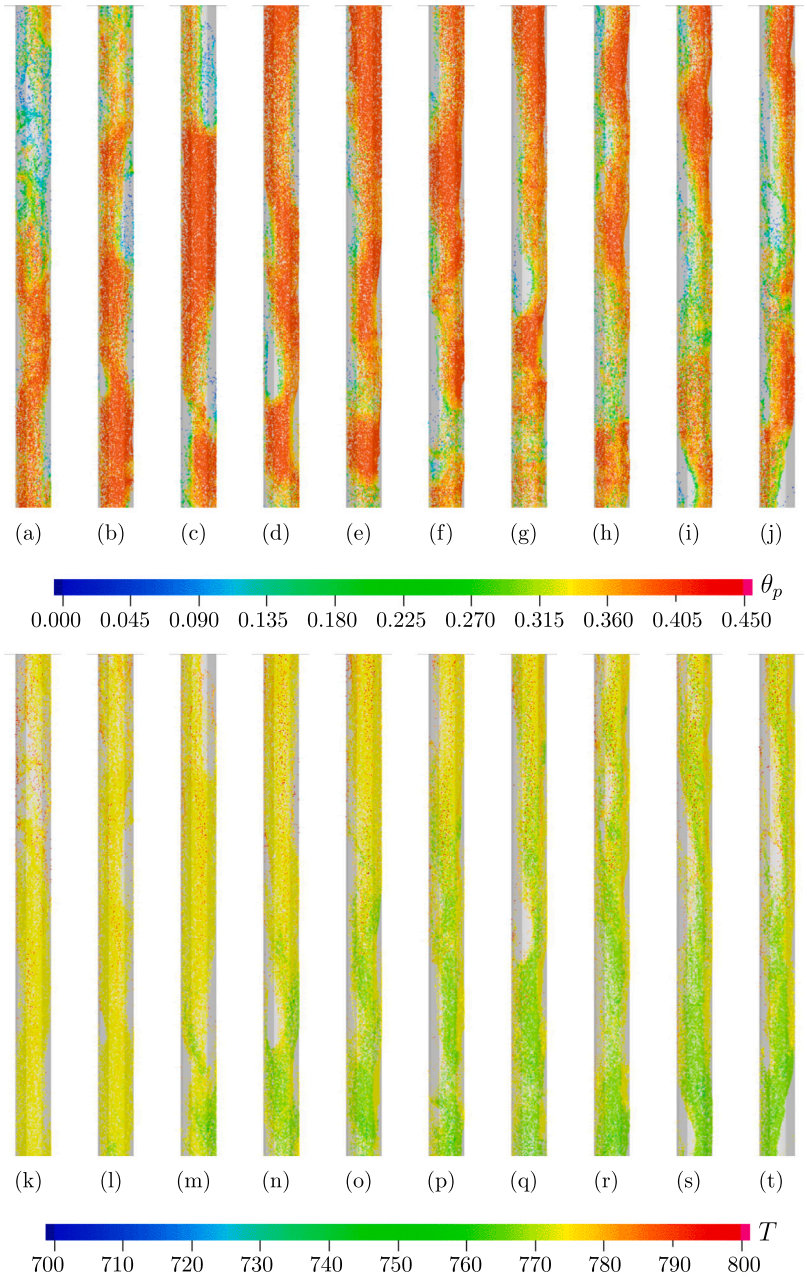

Fig. 9. Snapshots of particle volume fraction, θ_p and particle temperature, T, evolution in the heated length of the tube between $t = 179.1$ and $t = 180.0$ s with $\Delta t = 0.1$ s between figures. Temperature in Kelvin.

remains approximately constant at the initial temperature, $T = 500$ °C, although some fluctuations are observed. The temperature at the exit of the heated section increases to approximately $T_{x=1.55\,\mathrm{m}} = 540$ °C. Nevertheless, substantial variations in the temperature are observed during the simulation. At $t \approx 180$ s, there is a great reduction in both temperatures. Additionally, some reductions in the temperature at the outlet of the heated sections are observed at $t \approx 50$ s and $t =\approx 160$ s.

To explain these large temperature fluctuations, Figs. 11 and 12 show the cumulative mass of particles (defined in Eq. (17)) at the inlet and outlet sections and the heat transfer coefficient, defined as follows [12]:

$$h_w = \frac{\dot{Q}_w}{\left(\pi\, d\, L_{\mathrm{heat}}\right) \Delta T_{lm}} \tag{18}$$

where $\dot{Q}_w$ is the heat transferred from the hot wall to the particles, d is the internal diameter of the tube, and $L_{\mathrm{heat}} = 0.5$ m is the length of the tube at $T_w = 700$ °C, with

$$\Delta T_{lm} = \frac{\left(T_w - T_{p,x=1.05\,\mathrm{m}}\right) - \left(T_w - T_{p,x=1.55\,\mathrm{m}}\right)}{\ln\left(\dfrac{T_w - T_{p,x=1.05\,\mathrm{m}}}{T_w - T_{p,x=1.55\,\mathrm{m}}}\right)}$$

being the log mean temperature difference.

When the particle temperature is reduced ($t \approx 60, 160$ and 180 s), an increase in both mass flow-rate of particles and heat transfer coefficient can be clearly observed. Thus, the reduction in the particle temperature observed in Fig. 10 is related to a compact mass of particles with low voidage. Although the heat transfer rate increases, there is a larger mass of particles to heat up and, consequently, the temperatures at the outlet of the heated length are reduced.

The average in time heat transfer coefficient shown in Fig. 12 is $\bar{h}_w = 329\,\mathrm{W/(m^2\,K)}$. This heat transfer coefficient is lower than the values experimentally measured by Benoit et al. [12], who observed

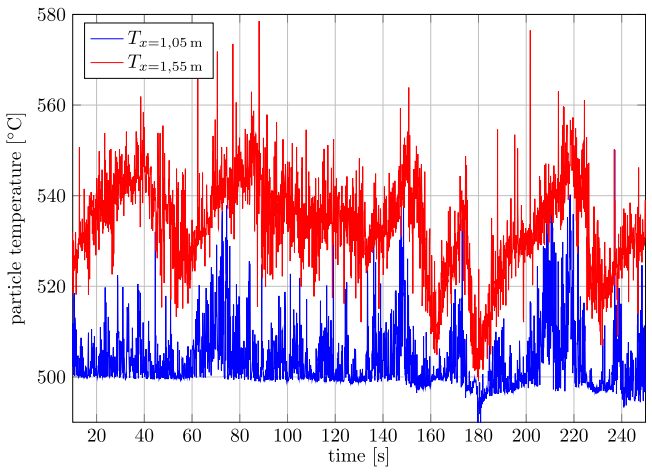

Fig. 10. Particle temperatures at the beginning ($x = 1.05\,m$) and at the end ($x = 1.55\,m$) of the heated section with $T_w = 700\,°C$ and $\Delta p_{bottom} = 32.2$ kPa.

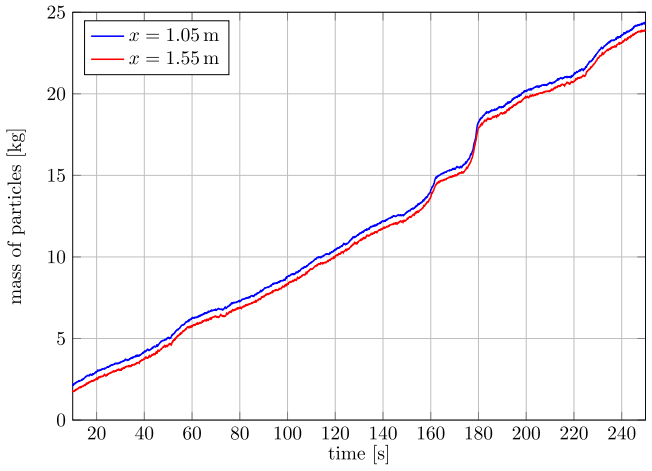

Fig. 11. Accumulated mass of particles through the cross-section of the tube at the beginning ($x = 1.05\,m$) and end ($x = 1.55\,m$) of the heated section with $T_w = 700\,°C$ and $\Delta p_{bottom} = 32.2$ kPa.

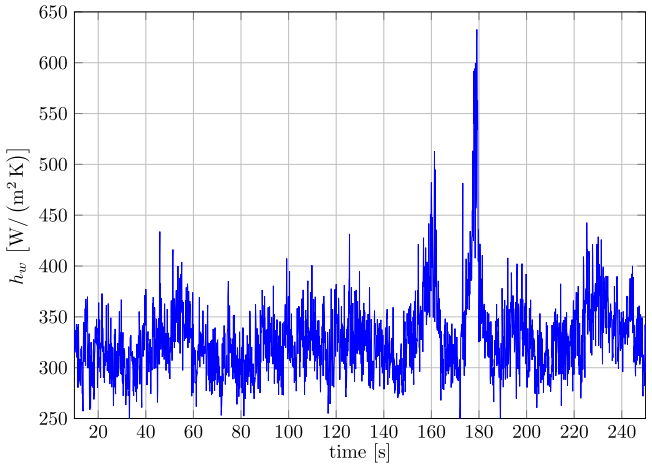

Fig. 12. Heat transfer coefficient at the wall of the heated section with $T_w = 700\,°C$ and $\Delta p_{bottom} = 32.2$ kPa.

values of $\bar{h}_w$ between 400 and 1200 W/(m² K) for solid mass flux in the range of $10 - 50\,kg/(s\,m^2)$. The mass flux of particles in the case shown in Figs. 9–12 was $104\,kg/(s\,m^2)$. These differences can be attributed to various factors. First, Benoit et al. [12] did not compute the average bulk temperature at the outlet of the heated length ($x = 1.55\,m$), but measured the local particle temperature at the centre of the tube. Second, and more importantly, Benoit et al. [12] computed heat transfer $\dot{Q}$ as the temperature increase from the bottom bed to the exit of the heated length. In the experimental facility, there was heat transfer by conduction along the vertical tube, and, arguably, the particles were heated from the bottom of the tube, as the high solar irradiation heated the length of the tube exposed directly to the concentrated irradiation. However, part of this heat is transferred by conduction along the vertical tube. In other words, Benoit et al. [12] computed the heat transferred to the particles from $x = 0$ up to $x = 1.55\,m$. This cannot be observed in the numerical simulation, as the tube thickness cannot be included in the simulation.

7. Discussion of results and future work

Future works should explore the inclusion of the tube thickness in the simulation, not only to compute the heat transfer by conduction in the tube, but also to determine the thermal stress suffered by a tube exposed to high levels of concentrated irradiation. In this work, a constant temperature boundary condition of $T_w = 700\,°C$ was imposed in the heated wall, due to the numerical model restrictions. However, when a tube is directly exposed to concentrated irradiation, wall temperature varies, with this being highest in the front of the tube (directly exposed to the irradiation) and lowest at the rear side of the tube. For example, [12] observed variations in the wall temperature of up to 160 °C. In addition, the proper boundary condition is to impose a solar flux distribution, with the maximum in the front and the minimum in the rear, rather than impose a temperature at the wall. For example, Rodríguez-Sánchez et al. [39] imposed a two-dimensional normal distribution with average and maximum heat flux of $0.8\,MW/m^2$ and $1.2\,MW/m^2$, respectively, which is that obtained with a three aiming point strategy.

Although the non-uniform heat flux along the heated tube may not notably influence the mean heat transfer coefficient h_w, it has a great impact on the thermal stress [39] and deflection, creep and fatigue of the tubes [40–42]. These previous works studied the mechanical damage of the tubes in conventional CSP plants with a central receiver operating with molten salts. In this case, under typical operating conditions, the heat transfer coefficient in the internal wall of the tube in contact with the fluid is in the range of $6 - 14 \times 10^3\,W/(m^2\,K)$ for molten salt velocities between 2 and 6 m/s, under non-uniform heat flux conditions [43]. These heat transfer coefficients are one order of magnitude higher than the typical values observed in dense suspension of particles [12]. Consequently, the mechanical damage expected in a tube filled with a dense suspension of particles should be higher than in a tube filled with a flowing fluid, such as molten salts. In addition, the heat flux experimentally tested with particles is approximately half of the typical heat flux in conventional CSP plants with molten salts, which is close to $1\,MW/m^2$. Thus, future experimental and numerical works related to externally irradiated tubes with particles should focus on studying the thermal and mechanical stress of the tubes, to test the long-term mechanical viability of the system. The preliminary results presented in this work predict thermal and mechanical problems in the tube due to the lower heat transfer rate, compared with molten salts, as well as the fluctuations observed on the up-flow of particles and the heat transfer coefficient in the internal surface of the tube.

8. Conclusions

The results presented in this work indicate that the MP-PIC method is able to predict the up-flow of particles in a vertical tube, as the numerical results (in the isothermal case) are highly consistent with the experimental data of Boissiere et al. [11] of up to $\dot{m}_p = 150\,kg/h$

with errors of ±10 kg/h. The numerical results indicate a significant influence of the overpressure at the bottom and of the aeration flow rate. Hence, the up-flow of particles at the exit increases notably for the cases with higher overpressure values (33.7 kPa and 34.7 kPa), approximately 8 and 12 times more than the case with the lowest Δp_{bottom} (31.7 kPa). Moreover, the total mass of particles increases as the aeration flow rate increases, in a range of 30% ($\dot{V}_{ae}$ = 40 NL/h) and 170% ($\dot{V}_{ae}$ = 150 NL/h), higher than the case without aeration flow rate.

The results obtained in the non-isothermal case predict a mean value of the heat transfer coefficient at the inner wall of the tube of $\bar{h}_w$ = 329 W/(m^2 K) under the conditions imposed in the numerical model. High fluctuations were observed in h_w during the transient process. The influence of these fluctuations on the creep and fatigue of the tube should be studied in detail in future works to ensure viability over long periods of the system. The numerical simulation shows the appearance of bubbles during the process, which notably influences the heat transfer exchange.

9. Notation

A_p Projected area of the particle [m^2]
A_t Cross-sectional area of the tube [m^2]
C_d Gas–particle drag coefficient
Cp_p Specific heat of the particle [J/(kg K)]
d Internal diameter of the tube [m]
D_p Drag function
d_p Particle diameter [m]
F Momentum exchange rate per volume between gas and particles [N/m^3]
F_p Drag force exerted on the particles [N]
f_p Function of the particle volume fraction at the wall
F_{wp} View factor between the wall and the particles in the adjacent cells [-]
g Gravity acceleration [m/s^2]
h_f Heat transfer coefficient of the gas[W/(m^2 K)]
h_{fe} Fluid enthalpy [J]
h_{fp} Fluid-to-particle heat transfer coefficient [W/(m^2 K)]
h_p Instantaneous convective heat transfer coefficient of the particles [W/(m^2 K)]
h_{pe} Particle enthalpy [J]
h_w Local fluid-to-wall heat transfer coefficient [W/(m^2 K)]
$\bar{h}_w$ Average in time heat transfer coefficient [W/(m^2 K)]
k_f Fluid thermal conductivity [W/(m K)]
k_p Particle thermal conductivity [W/(m K)]
L Cell length [m]
L_{heat} Length of the heated wall [m]
m_p Particle mass [kg]
$\dot{m}_{p,f}$ Up-flow of particles [kg/h]
Nu_f Nusselt number for heat transfer in the fluid to the particle
p Fluid pressure [Pa]
Pr Prandtl number
P_{out} Pressure outlet [Pa]
P_s Pressure constant
$\dot{Q}_{rad}$ Source term [W]
q Fluid heat flux [W/m^2]
$\dot{q}_D$ Enthalpy diffusion term associated with chemical reactions [W/m^3]
$\dot{Q}$ Energy source per volume [W/m^3]
$\dot{Q}_w$ Heat transferred from the hot wall to the particles [W]
R_g Gas constant [kJ/(kg K)]
Re Reynolds number
Sh Conservative energy exchange from the particle phase to the fluid phase [W/m^3]
T Absolute temperature [K]
T_x Temperature at location x [K]
T_f Fluid temperature [K]
T_p Particle temperature [K]
T_s Tube surface temperature [K]
T_w Wall temperature [K]
$\bar{T}_p$ Mass-weighted temperature of the particles [K]
T_{wb} Wall bed temperature [K]
u_f Fluid velocity [m/s]
u_{mf} Minimum fluidization velocity [m/s]
u_p Particle velocity [m/s]
V_p Particle volume [m^3]
$\dot{V}_{ae}$ Aeration flow rate [NL/h]

9.1. Greek symbols

β Constant
Δt Time interval [s]
ΔT_{lm} Logarithmic mean temperature difference [K]
Δp_{bottom} Over pressure at the bottom of the bed [kPa]
Δx Length interval [m]
ε Constant
ε_p Particle emissivity [-]
ε_w Wall emissivity [-]
θ_{cp} Particle volume fraction at close packing
θ_f Fluid volume fraction
θ_p Particle volume fraction
μ_f Dynamic viscosity of the fluid [kg/(m s)]
ρ_f Fluid density [kg/m^3]
ρ_p Particle density [kg/m^3]
σ Stefan–Boltzmann constant [W/m^2 K^4]
τ_f Fluid stress tensor [Pa]
τ_p Particle normal stress [Pa]
Φ Viscous dissipation [W/m^3]
Ψ_p Particle sphericity

CRediT authorship contribution statement

J.I. Córcoles: Conceptualization, Methodology, Software, Validation, Formal analysis, Data curation, Writing – original draft, Writing– review & editing, Visualization, Supervision, Project administration, Funding acquisition. **M. Díaz-Heras:** Conceptualization, Methodology, Formal analysis, Data curation, Writing – original draft, Writing– review & editing, Visualization. **M. Fernández-Torrijos:** Conceptualization, Methodology, Formal analysis, Data curation, Writing – original draft, Writing– review & editing, Visualization. **J.A. Almendros-Ibáñez:** Conceptualization, Methodology, Validation, Formal analysis, Data curation, Writing – original draft, Writing– review & editing, Visualization, Supervision, Project administration, Funding acquisition.

Declaration of competing interest

The authors declare that they have no known competing financial interests or personal relationships that could have appeared to influence the work reported in this paper.

Acknowledgements

This work was partially funded by the project PID2021-127322OB-I00, funded by the Ministerio de Ciencia e Innovación, Spain MICIN/AEI/10.13039/501100011033/ and by FEDER Una manera de hacer Europa; Project SBPLY/21/180501/000017, funded by the Regional Government of Castilla-La Mancha, Spain and by FEDER Una

manera de hacer Europa; Project RED2018-102431-T, funded by the Ministerio de Ciencia, Innovación *y* Universidades - Agencia Estatal de Investigación (AEI), Spain and Project 2020-GRIN-28725, funded by Universidad de Castilla-La Mancha, Spain.

References

[1] Renewables 2021. Analysis and forecast to 2026, Technical Report, International Energy Agency, 2021.
[2] Y.L. He, Y. Qiu, K. Wang, F. Yuan, W.Q. Wang, M.J. Li, J.Q. Guo, Perspective of concentrating solar power, Energy 198 (2020) 117373.
[3] L.F. Cabeza, E. Galindo, C. Prieto, C. Barreneche, A.I. Fernández, Key performance indicators in thermal energy storage: Survey and assessment, Renew. Energy 83 (2015) 820–827.
[4] J.A. Almendros-Ibáñez, M. Fernández-Torrijos, M. Díaz-Heras, J. Belmonte, C. Sobrino, A review of solar thermal energy storage in beds of particles: Packed and fluidized beds, Sol. Energy 192 (2019) 193–237.
[5] C.K. Ho, A review of high-temperature particle receivers for concentrating solar power, Appl. Therm. Eng. 109 (2016) 958–969.
[6] L.F. González-Portillo, R. Abbas, K. Albrecht, C. Ho, Analysis of optical properties in particle curtains, Sol. Energy 213 (2021) 211–224.
[7] W. Wu, D. Trebing, L. Amsbeck, R. Buck, R. Pitz-Paal, Prototype testing of a centrifugal particle receiver for high-temperature concentrating solar applications, J. Sol. Energy Eng. 137 (4) (2015).
[8] M. Díaz-Heras, A. Calderón, M. Navarro, J. A. Almendros-Ibañez, A. I. Fernández, C. Barreneche, Characterization and testing of solid particles to be used in CSP plants: Aging and fluidization tests, Sol. Energy Mater. Sol. Cells 219 (2021) 110793.
[9] M. Díaz-Heras, C. Barreneche, J. F. Belmonte, A. Calderón, A. I. Fernández, J. A. Almendros-Ibáñez, Experimental study of different materials in fluidized beds with a beam-down solar reflector for CSP applications, Sol. Energy 211 (2020) 683–699.
[10] T. Tan, Y. Chen, Z. Chen, N. Siegel, G.J. Kolb, Wind effect on the performance of solid particle solar receivers with and without the protection of an aerowindow, Sol. Energy 83 (10) (2009) 1815–1827.
[11] B. Boissiere, R. Ansart, D. Gauthier, G. Flamant, M. Hemati, Experimental hydrodynamic study of gas-particle dense suspension upward flow for application as new heat transfer and storage fluid, Can. J. Chem. Eng. 93 (2) (2015) 317–330.
[12] H. Benoit, I.P. López, D. Gauthier, J.-L. Sans, G. Flamant, On-sun demonstration of a 750 C heat transfer fluid for concentrating solar systems: Dense particle suspension in tube, Sol. Energy 118 (2015) 622–633.
[13] K. Jiang, Y. Kong, C. Xu, Z. Ge, X. Du, Experimental performance of gas-solid countercurrent fluidized bed particle solar receiver with high-density suspension, Appl. Therm. Eng. (2022) 118661.
[14] D. Kunii, O. Levenspiel, Fluidization Engineering, Butterworth-Heinemann, 1991.
[15] Y. Deng, F. Sabatier, R. Dewil, G. Flamant, A. Le Gal, R. Gueguen, J. Baeyens, S. Li, R. Ansart, Dense upflow fluidized bed (DUFB) solar receivers of high aspect ratio: Different fluidization modes through inserting bubble rupture promoters, Chem. Eng. J. 418 (2021) 129376.
[16] H. Benoit, R. Ansart, H. Neau, P. Garcia Triñanes, G. Flamant, O. Simonin, Three-dimensional numerical simulation of upflow bubbling fluidized bed in opaque tube under high flux solar heating, AIChE J. 64 (11) (2018) 3857–3867.
[17] K. Jiang, Z. Tian, S. Chen, C. Xu, X. Du, Numerical simulation on gas-solid flow characteristics in a high-density countercurrent fluidized bed particle solar receiver, Sol. Energy 249 (2023) 387–400.
[18] J.I. Córcoles, A. Acosta-Iborra, J.A. Almendros-Ibáñez, Influence of immersed surface shape on the heat transfer process and flow pattern in a fluidized bed using numerical simulation., Int. J. Heat Mass Transfer 178 (2021) 121621.
[19] J.I. Córcoles, A. Acosta-Iborra, J.A. Almendros-Ibáñez, C. Sobrino, Numerical simulation of a 3-D gas-solid fluidized bed: Comparison of TFM and CPFD numerical approaches and experimental validation, Adv. Powder Technol. 32 (10) (2021) 3689–3705.
[20] Y. Liang, Y. Zhang, T. Li, C. Lu, A critical validation study on CPFD model in simulating gas–solid bubbling fluidized beds, Powder Technol. 263 (2014) 121–134.
[21] T.B. Anderson, R. Jackson, Fluid mechanical description of fluidized beds. Equations of motion, Ind. Eng. Chem. Fundam. 6 (4) (1967) 527–539.
[22] D. Snider, An incompressible three-dimensional multiphase particle-in-cell model for dense particle flows, J. Comput. Phys. 170 (2) (2001) 523–549.
[23] J. Smagorinsky, General circulation experiments with the primitive equations: I. The basic experiment, Mon. Weather Rev. 91 (3) (1963) 99–164.
[24] F.A. Williams, Combustion theory benjamin, Cummings, Menlo Park (1985).
[25] J.-H. Lim, K. Bae, J.-H. Shin, J.-H. Kim, D.-H. Lee, J.-H. Han, D.H. Lee, Effect of particle–particle interaction on the bed pressure drop and bubble flow by computational particle-fluid dynamics simulation of bubbling fluidized beds with shroud nozzle, Powder Technol. 288 (2016) 315–323.
[26] P.J. O'Rourke, Collective drop effects on vaporizing liquid sprays, Technical Report, Los Alamos National Lab., NM (USA), 1981.
[27] D.M. Snider, S.M. Clark, P.J. O'Rourke, Eulerian–Lagrangian method for three-dimensional thermal reacting flow with application to coal gasifiers, Chem. Eng. Sci. 66 (6) (2011) 1285–1295.
[28] C.Y. Wen, Mechanics of fluidization, in: Chem. Eng. Prog. Symp. Ser., vol. 62, 1966, pp. 100–111.
[29] S. Karimipour, T. Pugsley, Application of the particle in cell approach for the simulation of bubbling fluidized beds of Geldart A particles, Powder Technol. 220 (2012) 63–69.
[30] W.-c. Yang, Handbook of Fluidization and Fluid-Particle Systems, CRC Press, 2003.
[31] M. Leva, M. Grummer, A correlation of solids turnover in fluidized systems-its relation to heat transfer, Chem. Eng. Progress 48 (6) (1952) 307–313.
[32] W.J.M. Douglas, S.W. Churchill, Recorrelation of data for convective heat-transfer between cases and single cylinders with large termperature differences, 1955.
[33] R. Turton, T. Fitzgerald, O. Levenspiel, An experimental method to determine the heat transfer coefficient between fine fluidized particles and air via changes in magnetic properties, Int. J. Heat Mass Transfer 32 (2) (1989) 289–296.
[34] G.F. Hewitt, G.L. Shires, T. Bott, Process Heat Transfer, Begell House, 1994.
[35] M. Sommerfeld, N. Huber, Experimental analysis and modelling of particle-wall collisions, Int. J. Multiph. Flow. 25 (6–7) (1999) 1457–1489.
[36] M. Nakhaei, C.E. Hessel, H. Wu, D. Grévain, S. Zakrzewski, L.S. Jensen, P. Glarborg, K. Dam-Johansen, Experimental and CPFD study of gas–solid flow in a cold pilot calciner, Powder Technol. 340 (2018) 99–115.
[37] S. Kraft, M. Kuba, F. Kirnbauer, K. Bosch, H. Hofbauer, Optimization of a 50 MW bubbling fluidized bed biomass combustion chamber by means of computational particle fluid dynamics, Biomass Bioenergy 89 (2016) 31–39.
[38] V. Barracuda, User Guide, CPFD. TX,USA, 2022.
[39] M.R. Rodríguez-Sánchez, A. Soria-Verdugo, J.A. Almendros-Ibáñez, A. Acosta-Iborra, D. Santana, Thermal design guidelines of solar power towers, Appl. Therm. Eng. 63 (1) (2014) 428–438.
[40] P. González-Gómez, M.R. Rodríguez-Sánchez, M. Laporte-Azcué, D. Santana, Calculating molten-salt central-receiver lifetime under creep-fatigue damage, Sol. Energy 213 (2021) 180–197.
[41] M. Laporte-Azcué, P. González-Gómez, M.R. Rodríguez-Sánchez, D. Santana, Material selection for solar central receiver tubes, Sol. Energy Mater. Sol. Cells 231 (2021) 111317.
[42] M. Laporte-Azcué, P. González-Gómez, M.R. Rodríguez-Sánchez, D. Santana, Deflection and stresses in solar central receivers, Sol. Energy 195 (2020) 355–368.
[43] Z. Ying, B. He, L. Su, Y. Kuang, D. He, C. Lin, Convective heat transfer of molten salt-based nanofluid in a receiver tube with non-uniform heat flux, Appl. Therm. Eng. 181 (2020) 115922.